ACS Sustainable Chemistry & Engineering

Research Article

pubs.acs.org/journal/ascecg

Microwave Hydrothermal Synthesis of Ni-based Metal–Organic Frameworks and Their Derived Yolk–Shell NiO for Li-Ion Storage and Supported Ammonia Borane for Hydrogen Desorption

Shaofeng Kong, Ruoling Dai, Hao Li, Weiwei Sun,* and Yong Wang*

Department of Chemical Engineering, School of Environmental and Chemical Engineering, Shanghai University, Shangda Road 99, Shanghai, P. R. China, 200444

Supporting Information

ABSTRACT: This paper reports fast microwave hydrothermal synthesis of Ni-based metal–organic frameworks (Ni-MOFs) and their derived yolk–shell NiO structures by direct calcination in air. The molar ratio of the Ni ion to the benzene-1,3,5-tricarboxylic acid (H_3BTC) ligand has important influence on the NiO morphologies and their electrochemical performances. The obtained yolk–shell NiO microsphere displays a large reversible capacity of 1060 mAh g^{-1} at a small current density of 0.2 A g^{-1} and a good high-rate capability when evaluated as an anode for rechargeable lithium-ion batteries. Moreover, the facilitated hydrogen release from ammonia borane (AB) at a lower temperature and the depressed release of undesired volatile byproducts are also observed in the Ni-MOFs supported AB.

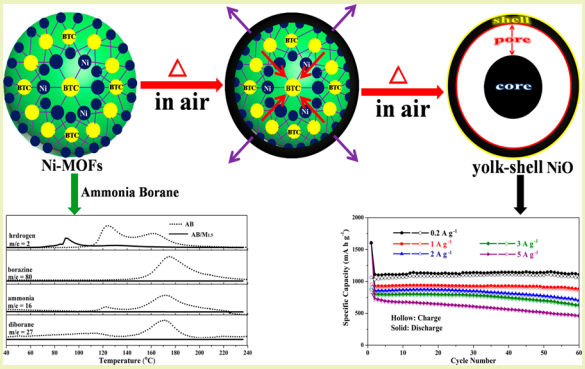

KEYWORDS: *Yolk–shell, NiO, Metal–organic frameworks, Lithium-ion battery, Hydrogen desorption*

INTRODUCTION

There is a increasing demand to make efficient use of energy and to find renewable and clean energy sources that can substitute for fossil fuels.[1,2] Energy storage, an important intermediate step toward versatile, clean, and efficient energy applications, has received worldwide concern both in academia and industry.[3−7] Among various candidates of energy storage systems, lithium-ion batteries (LIB) and fuel cells have received considerable attention owing to their high energy densities and environmental benignity.[8−16] LIB, one of the most important rechargeable batteries, have been widely used due to their high energy density and long cycle life.[10,17,18] Metal oxides such as NiO have long been extensively investigated as a potential electrode material for LIBs because of their 2−3 times higher theoretical capacities than commercial graphite electrodes.[19−42] However, their cycling performances and high-rate capabilities are still not satisfactory due to the large volume change associated with lithium insertion and extraction and poor electrical conductivity.[32−38,40−42] Hydrogen is one of the most promising candidates to replace nonrenewable fuel sources because it can react with oxygen to generate electricity with high energy density without byproducts.[43−45] Thus, hydrogen has been regarded as a suitable energy carrier for energy production from primary sources. Advanced materials are highly desired that can store a large amount of hydrogen at mild conditions (common temperature and relatively low pressure) along with a fast release kinetics.[46] Over the past decade, ammonia borane (NH_3BH_3, AB) has received much attention as a solid-state hydrogen storage medium because of its satisfactory stability, relatively low molecular mass, and remarkably high energy density.[47−50] However, its practical application is greatly limited by the poor kinetics of hydrogen generation below 85 °C and the release of impurities that are detrimental to fuel cells.

Metal–organic frameworks (MOFs) are porous materials synthesized by assembling metal ions with organic bridging ligands.[51,52] The metal ions in the MOFs can be thermally transformed into metal oxides, and the C and other elements are oxidized into gas molecules after calcining the MOFs in air at elevated temperatures.[53] Through the topological conversion by thermal treatment, the corresponding metal oxides can be readily synthesized with a similar morphology to the nanoscale MOFs precursors and a certain degree of permanent porosity.[54−59] These pores generated by such a calcination process are typically hydrophobic, which are favorable to the infiltration of the electrolyte and Li^+ ion diffusion coefficient.[60] In particular, AB-filled MOFs have been recently synthesized from the self-assembly of metal clusters and organic molecules into an infinite array, and they showed enhanced dehydrogenation properties of AB.[61−64]

Herein, this work presents a fast and facile microwave hydrothermal method to synthesize Ni-MOFs from nickel

Received: May 9, 2015
Revised: June 25, 2015
Published: July 6, 2015

ACS Publications © 2015 American Chemical Society

DOI: 10.1021/acssuschemeng.5b00556
ACS Sustainable Chem. Eng. 2015, 3, 1830−1838

nitrate and benzene-1,3,5-tricarboxylic acid (H_3BTC). There are two main objectives in this work for applications of the obtained Ni-MOFs. The primary objective is to use the Ni-MOF as the precursor to obtain a yolk−shell NiO microsphere for Li-ion battery application. Owing to its mesoporous structure, the yolk−shell NiO exhibited enhanced electrochemical performances compared to other NiO nanostructures. A large reversible capacity of ~1060 mAh g^{-1} could be achieved at a small current density of 0.2 A g^{-1} along with a good high-rate cycling performance. The secondary objective is to use the Ni-MOFs as the matrix to support ammonia borane (AB). Nickel ions are also used as the catalyst to promote the latter's hydrogen desorption property. The obtained Ni-MOF/AB composite delivered improved hydrogen desorption properties with a low dehydrogenation temperature of ~70 °C. Those byproducts such as ammonia and diborane/borazine were also effectively prevented.

EXPERIMENTAL SECTION

Materials Preparation. *Preparation of Ni-MOFs.* $Ni(NO_3)_2 \cdot 6H_2O$ and a calculated amount of benzene-1,3,5-tricarboxylic acid (H_3BTC) (theoretical molar ratios of Ni:H_3BTC are 1:1, 1.5:1, 2:1, and 2.5:1) were mixed and dissolved in 15 mL dimethylformamide (DMF). The obtained green solution was transferred into a specialized glass tube and followed by microwave irradiation with continuous magnetic stirring in a single mode microwave reactor (Nova, EU Microwave Chemistry) at 150 °C for 30 min. After cooling to room temperature, the product was collected by centrifugation, washed copiously with DMF and ethanol, and dried in a vacuum oven at 60 °C for 12 h. The obtained samples prepared from different molar ratios of Ni:H_3BTC of 1:1, 1.5:1, 2:1, and 2.5:1 were labeled as M_1, $M_{1.5}$, M_2, and $M_{2.5}$, respectively.

Preparation of Yolk−Shell NiO Microspheres. Green Ni-MOFs powders were placed in a tube furnace and heated at 500 °C for 2 h in air. The obtained black powder was NiO and labeled as N_1, $N_{1.5}$, N_2, and $N_{2.5}$, corresponding to various Ni-MOFs precursors (M_1, $M_{1.5}$, M_2, and $M_{2.5}$). As a benchmarked sample, NiO nanoparticles (N_0) were also synthesized by calcining $Ni(NO_3)_2 \cdot 6H_2O$ in the absence of H_3BTC via a similar process.

Preparation of AB@Ni-MOFs. Typically, 50 mg of Ni-MOFs ($M_{1.5}$) was heated at 100 °C for 6 h under vacuum to remove the coordinated water molecules and then mixed with 50 mg ammonia borane (AB). The mixture was sealed in an argon-filled 100 mL hardened steel bowl and ball-milled at 300 rpm for 2h. The obtained Ni-MOFs loaded AB composite was named as AB@$M_{1.5}$. Because of the sensitivity of AB to oxygen and moisture, the sample of AB@$M_{1.5}$ was weighed and stored in an argon-filled glovebox, which kept both water and oxygen concentrations below 1 ppm during operation.

Materials Characterization. The products were characterized by X-ray diffraction (XRD, Rigaku D/max-2550 V, Cu Kα radiation), field-emission scanning electron microscopy (FE-SEM, JSM-6700F) with an energy-dispersive X-ray spectrometer (EDS), and transmission electron microscopy/selected area electron diffraction (TEM/SAED, JEOL JEM-200CX, and JEM-2010F). The specific surface area and porous structures were characterized by an accelerated surface area and porosimetry analyzer (Micromeritics Instrument Corp, ASAP 2020 M +C, analysis adsorptive: Nitrogen). Fourier transform infrared (FTIR) spectra were measured by a BIO-RAD FTS 135 FTIR spectrophotometer using the KBr pellet method.

Electrochemical Measurement. Electrochemical performances were measured using two-electrode cells at a temperature of 20 °C. These cells were assembled in an argon-filled glovebox. The working electrode was composed of 80 wt % active materials, 10 wt % each of the conductive agent (acetylene black), and the binder (poly vinylidene difluoride, PVDF, Aldrich). The loading amount of the electrode on copper foil was around 1.5 mg cm^{-2}. Lithium foil (China Energy Lithium Co., Ltd.) was used as the counter and reference electrode, and polypropylene film (Celgard-2300) was used as separator. The electrolyte was 1 M $LiPF_6$ in a 50:50 w/w mixture of ethylene carbonate (EC) and diethyl carbonate (DEC). Electrochemical measurement was performed on a LAND CT2001 test system. The Swagelok-type cells were discharged (lithium insertion) and charged (lithium extraction) at a constant current (0.2 A g^{-1}) in the fixed voltage range of 5 mV to 3.0 V. Higher current densities (1, 2, 3, and 5 A g^{-1}) were also used, and the first cycle discharging was kept at 0.2 A g^{-1}. Cyclic voltammetry (CV) was carried out on a CH Instruments electrochemical workstation (model 660D) at a scan rate of 0.1 mV s^{-1}.

Hydrogen Release Measurements. The simultaneous thermogravimetry and mass spectrometry (TGA/MS, Netzsch STA 409C) measurements were carried out to investigate the heat effect and gaseous products at a heating rate of 5 °C per min from room temperature to 240 °C in argon atmosphere. The isothermal temperature-programmed desorption (TPD) was performed by Sievert's method under the temperature of 90 °C.

RESULTS AND DISCUSSION

Materials Synthesis and Characterization. Microwave syntheses have been widely used in material science due to their facile, fast, and energy-saving characteristics.[8] Single-mode microwave irradiation was used in this work to prepare Ni-MOFs because it can offer a more homogeneous reaction environment compared to a multimode commercial microwave oven and therefore help to obtain various metal/metal oxide products with uniform dispersion and size and morphology control.[8,10] It is worth noting that the reaction time is only 30 min, which is substantially reduced compared to previous long-time (24 h) formation of Ni-MOFs by a solvothermal route in electrical oven.[54] The crystallographic structure and phase purity of products were analyzed by XRD and FTIR, as shown in Figure 1a and Figure S1 of the Supporting Information. The diffraction pattern of the synthesized $M_{1.5}$ precursor (Ni-MOFs with the molar ratio of Ni:H_3BTC being 1.5:1) exhibits a largely amorphous nature, which is similar to previous Ni-MOFs.[54] Furthermore, two peaks at 1618 and 1553 cm^{-1} are observed in the FTIR curve of $M_{1.5}$ in Figure S1 of the Supporting Information, which can be assigned to the C═O and aromatic C═C functional groups of the BTC ligands. The XRD pattern of NiO ($N_{1.5}$) prepared by the thermal treatment of $M_{1.5}$ is also shown in Figure 1a. All diffraction peaks can be indexed to the (111), (200), (220), (311), and (222) planes, which are in good agreement with the standard face-centered cubic (fcc) NiO phase (PDF 47-1049).[27] No other impurity peaks are observed, indicating a complete thermal conversion from Ni-MOF precursors to NiO nanostructures in air. Figure 1b shows XRD patterns of the benchmarked NiO product (N_0) prepared directly from nickel nitrate and other NiO products (N_1, N_2, $N_{2.5}$) obtained from Ni-MOFs with different molar ratios of Ni to H_3BTC. These samples all exhibit same fcc phase to that of $N_{1.5}$.

The thermal transformation process from Ni-MOFs to NiO was investigated by thermogravimetric analysis (TGA), as shown in Figure 2a. The first-step of weight loss (4.6%) takes place from room temperature to 100 °C, corresponding to the removal of lattice water from Ni-MOFs, while the second-step of weight loss (22.3%) below 350 °C can be attributed to the removal of DMF solvent.[55,59] The subsequent heating in air results in the complete decomposition of Ni-MOFs and the formation of NiO. This process occurs in a temperature range from 350 to 435 °C with a dramatic weight loss of 47.2%. When the temperature continues to increase, there is no detected thermal event. It is indicated that NiO can be formed

DOI: 10.1021/acssuschemeng.5b00556
ACS Sustainable Chem. Eng. 2015, 3, 1830−1838

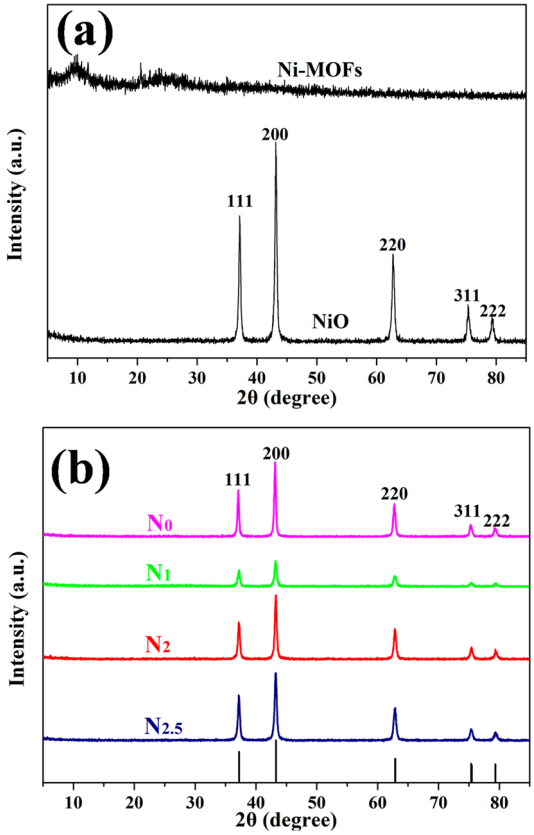

Figure 1. (a) XRD patterns of Ni-MOFs ($M_{1.5}$ with Ni:H_3BTC = 1.5:1) and the corresponding NiO products ($N_{1.5}$). (b) XRD patterns of various NiO products (N_0, $Ni(NO_3)_2{\cdot}6H_2O$ only; N_1, Ni:H_3BTC = 1:1; N_2, Ni:H_3BTC = 2:1; $N_{2.5}$, Ni:H_3BTC = 2.5:1).

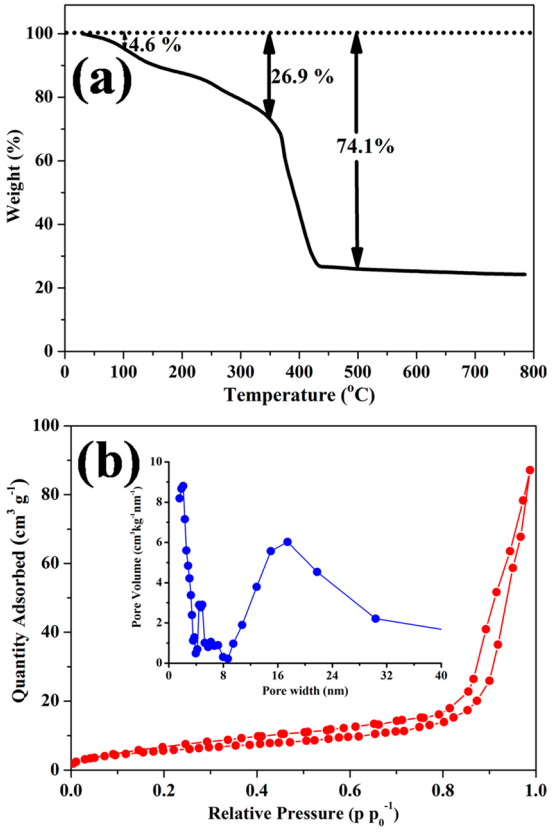

Figure 2. (a) TGA curve of Ni-MOFs of $M_{1.5}$ (Ni:H_3BTC = 1.5:1) in air. (b) Nitrogen adsorption−desorption isotherm of the yolk−shell NiO microsphere ($N_{1.5}$). Inset shows the pore size distribution.

below 435 °C. Therefore, a temperature of 500 °C in air was used to obtain crystalline NiO from Ni-MOFs in this work. Figure 2b shows the nitrogen adsorption/desorption isotherm curves of yolk−shell NiO microspheres. The specific Brunauer−Emmett−Teller (BET) surface area is 21.5 $m^2\ g^{-1}$, and their typical pore size distributions are ∼1−40 nm.

The morphology and microstructure of the as-prepared Ni-MOF precursors and NiO products were examined by scanning electron microscopy (SEM) and transmission electron microscopy (TEM). The SEM and magnified TEM images of the Ni-MOF ($M_{1.5}$) precursors are shown in Figure 3, which reveal the spherical morphology of the Ni-MOFs with diameters around 1−2 μm. Their surface is smooth under the low-magnification SEM imaging in Figure 3a. As indicated by the TEM image in Figure 3b, these Ni-MOF microspheres are solid without detected pores. After the one-step calcination of the $M_{1.5}$ precursor in air, the resulted NiO product ($N_{1.5}$) is shown in SEM images (Figure 4a−c) with various magnifications. In general, the similar microsphere morphology is observed for NiO with sphere size of ∼1−2 μm. As shown in the SEM image of a broken NiO microsphere in the inset of Figure 4b, it is worth noting that there is an internal NiO core, which is separated from the outer NiO shell in the microsphere. Moreover, the sphere surface is composed of innumerable small particles (Figure 4c), which presents a striking contrast to the smooth surface of Ni-MOF spheres. The TEM image in Figure 4d reveals more structural details of the spherical core: large void pores and shell layer of NiO microspheres. A unique yolk−shell NiO nanostructure can be clearly confirmed. Figure

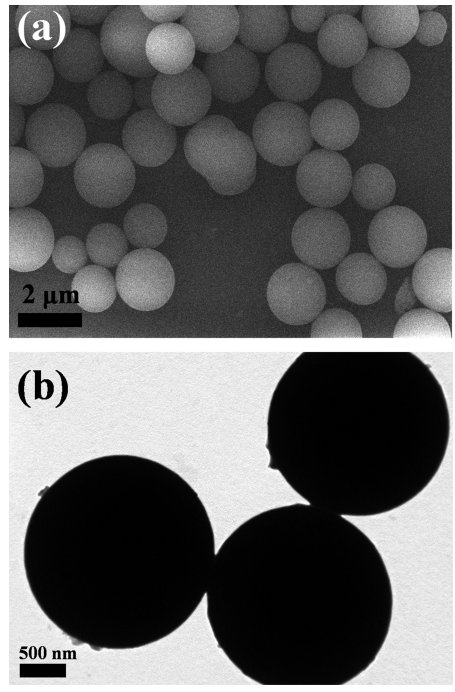

Figure 3. (a) SEM image and (b) TEM image for the Ni-MOF precursors of $M_{1.5}$.

5a−c shows elemental mapping images of NiO, which indicates the presence of uniform distribution of Ni and O elements.

DOI: 10.1021/acssuschemeng.5b00556
ACS Sustainable Chem. Eng. 2015, 3, 1830−1838

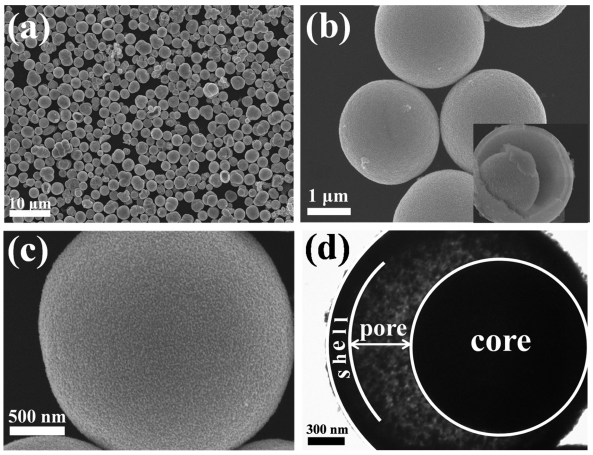

Figure 4. SEM images of NiO microsphere ($N_{1.5}$, Ni:H_3BTC = 1.5:1): (a) scale bar = 10 μm, (b) scale bar = 1 μm, and (c) scale bar = 500 nm. (d) TEM image of NiO microsphere ($N_{1.5}$).

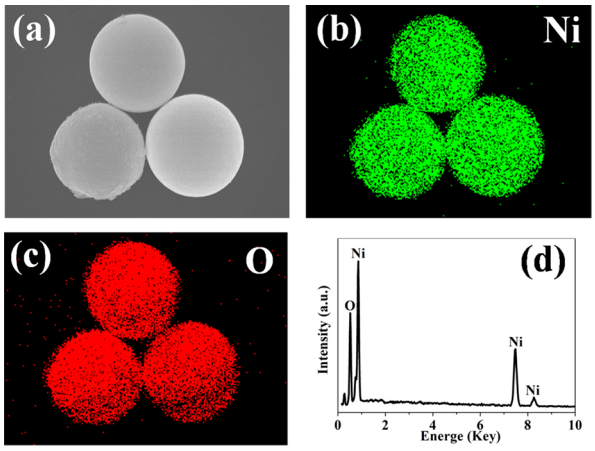

Figure 5. Elemental mapping images of $N_{1.5}$: (a) SEM image, (b) nickel element, (c) oxygen element. (d) EDS spectrum of $N_{1.5}$.

These elements can also be confirmed by the EDS results in Figure 5d.

The effect of molar ratio of Ni ion to H_3BTC on the MOFs-derived NiO products was also investigated. Almost all N_1 and N_2 products still exhibit microsphere morphology as shown in Figure 6a and b, respectively. A broken NiO microsphere (N_2) is shown in Figure 6c, which indicates the yolk–shell structure of NiO. This yolk–shell structure can also be confirmed by the TEM image of N_2 in Figure 6d. When the molar ratio of Ni to H_3BTC is further increased to 2.5, a mixture of microspheres and particles are observed in SEM image of $N_{2.5}$ in Figure 6e. The corresponding SEM image of a broken $N_{2.5}$ microsphere (Figure 6f) and TEM image (Figure 6g) also indicate there is a void space between the NiO shell and core. However, these pore spaces are largely reduced compared to the $N_{1.5}$ and N_2 products prepared from the Ni-MOFs with decreased molar ratios of Ni to H_3BTC. It is because the weight percentage of Ni in the Ni-MOF ($M_{2.5}$) precursor is the highest one among the $N_{1.5}$, N_2, and $N_{2.5}$ samples. The NiO product (N_0) prepared in the absence of H_3BTC is shown in Figure 6h; only nanoparticle products are observed. It is demonstrated that the amount of H_3BTC plays an important role in the product morphology.

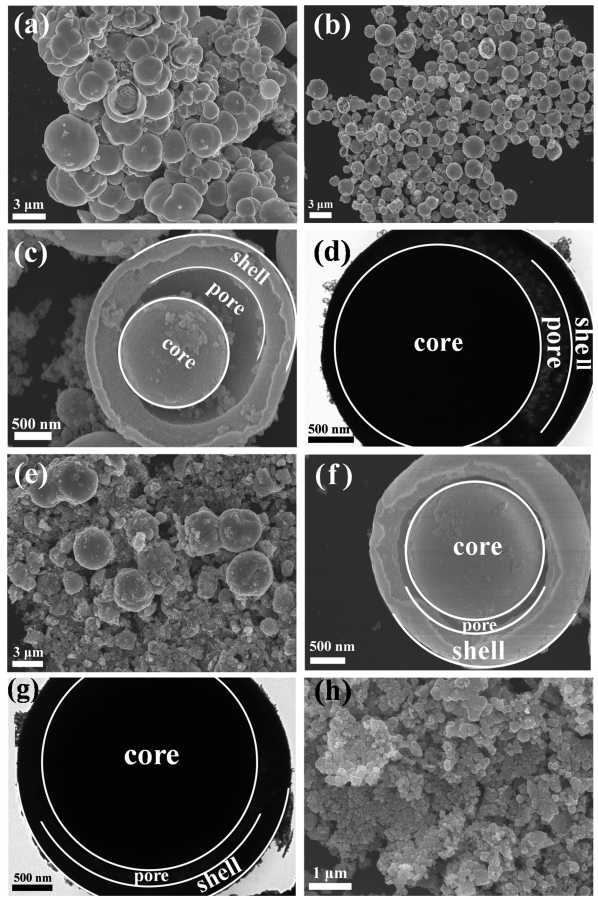

Figure 6. (a) SEM image of N_1, (b) SEM image of many N_2 microspheres, (c) SEM image of a broken N_2 microsphere, (d) TEM image of N_2, (e) SEM image of many $N_{2.5}$ microspheres, (f) SEM image of a broken $N_{2.5}$ microsphere, (g) TEM image of $N_{2.5}$, and (h) SEM image of N_0 without H_3BTC.

On the basis of the above results, the yolk–shell NiO microspheres can be obtained with morphology and size control by a MOF-based technique. Scheme 1 illustrates the overall strategy for the preparation of yolk–shell NiO microspheres, involving the fast microwave-assisted fabrication of Ni-MOF microspheres and subsequent calcination treatment at 500 °C in air. First, the Ni-MOF microspheres are prepared via a microwave-assisted hydrothermal method using Ni-$(NO_3)_2{\cdot}6H_2O$ and H_3BTC. Second, the subsequent thermal treatment leads to the transformation of Ni-MOFs into yolk–shell NiO microspheres. The formation of the yolk–shell structure is basically ascribed to the heterogeneous decomposition and contraction process of Ni-MOFs induced by nonequilibrium heat conduction. At the beginning of the calcination process, there is a large temperature gradient

Scheme 1. Schematic Illustration of Evolution of Yolk–Shell NiO Microspheres

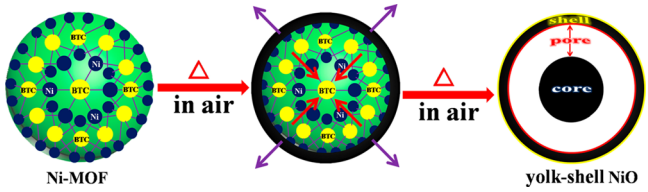

DOI: 10.1021/acssuschemeng.5b00556
ACS Sustainable Chem. Eng. 2015, 3, 1830–1838

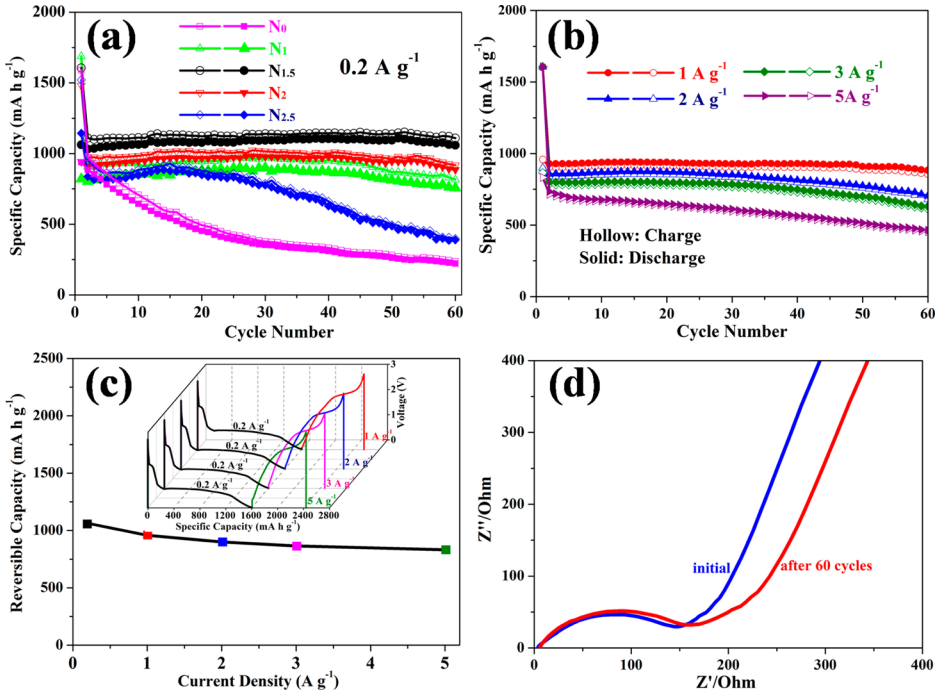

Figure 7. (a) Cycling performances of various NiO nanostructures (N_0, N_1, $N_{1.5}$, N_2, and $N_{2.5}$) at 0.2 A g^{-1}. (b) High-rate cycling performances of the yolk–shell NiO of $N_{1.5}$. (c) High-rate capabilities of $N_{1.5}$ anode. Inset figure is the first cycle discharge–charge curves at large currents. (d) Nyquist plots of $N_{1.5}$ anode.

existing along the radial direction from the exterior surface to interior core.[53] This leads to the surface decomposition of Ni-MOFs and the formation of a NiO shell. When the thermal treatment continues, the Ni-MOF core is further decomposed and changed to NiO. At this stage, there are two opposite forces. One is the outward force caused by the linkage between NiO shell and Ni-MOF core and the release of gas in the NiO-MOFs decomposition process. Another is the inward force caused by the decomposition and contraction of the Ni-MOF core.[56] Finally, after 2 h calcination treatment in air at 500 °C, the NiO shell and core are formed and separated by the void pores, forming a unique yolk–shell NiO microsphere nanostructure.

Lithium Storage Properties of MOFs-Derived NiO. It is believed that the unique porous yolk–shell NiO microspheres may hold certain merits as an anode for lithium-ion batteries. Their electrochemical lithium storage properties were performed by using the standard half-cell configuration. CV curves of the initial three cycles were first employed to evaluate Li storage electrochemical reactions of the porous NiO electrode ($N_{1.5}$) at a sweep rate of 0.1 mV s^{-1} and a voltage range from 0 to 3.0 V (Figure S2a, Supporting Information). In the first cathodic scan, a strong peak centered at ~0.45 V is related to the reduction reaction of NiO to Ni and the formation of amorphous Li_2O and a solid electrolyte interface (SEI). There is a peak at ~2.28 V in the first anodic scan, which should be assigned to the formation of NiO.[19,20,22,23] In the subsequent two cycles, the cathodic and anodic peaks can be found at 1.08 and 2.28 V, respectively. The second cycle is almost overlapped with the third cycle, indicating a high degree of reaction reversibility.[19,26] As shown in the initial three discharge (lithium insertion) and charge (lithium extraction) curves of the yolk–shell $N_{1.5}$ composite at a current density of 0.2 A g^{-1} (Figure S2b, Supporting Information), the discharge and charge capacities in the first cycle are 1606 and 1063 mAh g^{-1}, respectively. A Columbic efficiency (ratio of the lithium extraction capacity to the lithium insertion capacity) of ~66% can be determined. This large irreversible capacity loss in the first cycle should be ascribed to the electrolyte decomposition and the formation of solid electrolyte interface (SEI) film, which has also been observed in previous NiO anodes.[19−22] It is found that there is a long voltage plateau appeared at ~0.65 V in the first discharge process. In the subsequent discharge and charge cycles, the plateau is shifted to ~1.15 V, which is in agreement with the CV results mentioned above.

Figure 7a shows the cycling performances of the obtained NiO products at a current density of 0.2 A g^{-1}; all samples (N_1, $N_{1.5}$, N_2, and $N_{2.5}$) display better cycling stabilities than the N_0 sample prepared directly from nickel nitrate in the absence of H_3BTC. The yolk–shell $N_{1.5}$ microspheres exhibit the best cycling performances among all samples. They deliver an initial charge (lithium extraction) capacity of 1063 mAh g^{-1}, and there is almost no capacity fading during cycling. A high charge capacity of 1060 mAh g^{-1} could be still retained after 60 cycles, which corresponds to a retention rate of ~99.7% compared to the first cycle charge capacity. The average capacity fading rate is calculated to be only 0.005% per cycle. The large retained reversible capacity (1060 mAh g^{-1}) is larger than those of N_1 (756 mAh g^{-1}), N_2 (886 mAh g^{-1}), $N_{2.5}$ (389 mAh g^{-1}), and N_0 (221 mAh g^{-1}) after the same cycle number (60 cycles). This should be ascribed to good control of the uniform yolk–shell structure with enough pore cavities in the $N_{1.5}$ product. Compared with previous NiO anodes with various nanostructures such as nanoparticles, hollow microspheres, nanosheets, nanoflakes, and nanoflowers (Table S1, Supporting Information), the unique yolk–shell NiO of this work also exhibits enhanced lithium storage performance with larger reversible capacity.

High-rate cycling performances of yolk–shell $N_{1.5}$ microspheres were also tested at large current densities of 1, 2, 3, and

DOI: 10.1021/acssuschemeng.5b00556
ACS Sustainable Chem. Eng. 2015, 3, 1830−1838

5 A g^{-1} (Figure 7b). The $N_{1.5}$ product exhibits stable cycling performance at a large current of 1 A g^{-1}. The initial reversible charge capacity is 959 mAh g^{-1}, which decreases to 856 mAh g^{-1} after 60 cycles. The capacity fading is calculated to be 0.18% per cycle. With the increase in current densities, the yolk−shell $N_{1.5}$ microsphere exhibits decreased capacity and faster capacity fading. Reversible capabilities of 678, 612, and 454 mAh g^{-1} could be observed after 60 cycles at large current densities of 2, 3, and 5 A g^{-1} respectively. Figure 7c shows the high-rate capability of the yolk−shell $N_{1.5}$ microsphere. There is only a small decrease in the initial charge capacity when the current increases from 1 to 5 A g^{-1}. An excellent high-rate capability can be determined; for example, an initial charge capacity of 833 mAh g^{-1} can be observed at 5 A g^{-1}, which corresponds to 78.36% of the value achieved at 0.2 A g^{-1}. These good electrochemical properties should be ascribed to the unique yolk−shell structure of mesoporous NiO microspheres. Because the NiO core and shell are both composed of many small nanoparticles, there are pores among these nanoparticle-assembled NiO networks. These interstices among porous nanoparticle shells and cores are more convenient for the intercalation of Li^+ ions into active materials. The transport pathways of lithium ions are shortened, and electrochemical kinetics can be improved.[55] There are also large interior void spaces for the yolk−shell NiO microspheres as well as interparticle pores. These pore spaces can be used to efficiently buffer the stress caused by volume changes during the charge−discharge cycling, thus maintaining the mechanical integrity and electrical conductivity of the electrode material.

To further understand the outstanding electrochemical performance of the yolk−shell NiO nanostructure, an electrochemical impedance spectra (EIS) test was carried out in the frequency range from 0.01 Hz to 100 kHz at ambient temperature (Figure 7d). Apparently, the curvature of the semicircle remains nearly unchanged for the first and 60th cycles, indicating stable electrical conductivity, charge transfer, and electrochemical reactions during repetitive cycling. Moreover, the microsphere structure can be clearly observed in Figure S3 of the Supporting Information. The yolk−shell $N_{1.5}$ microsphere structures preserve the stable structure integrity after repetitive discharge−charge cycles. The successful demonstration of the yolk−shell NiO anode with enhanced Li-ion storage properties in this work may be also meaningful to design other types of high-capacity anodes such as Si and Sn.[2,6,8] These two elements have higher electrochemical activities because each of them can alloy and dealloy with a maximum 4.4 Li and therefore deliver much larger theoretical capacities of 4200 mAh g^{-1} (Si) and 990 mAh g^{-1} (Sn) than NiO.

Hydrogen Desorption Properties of MOFs-Supported AB. Mass spectrometry (MS) was used to compare the temperature profiles of volatile products (hydrogen, ammonia, diborane, and borazine) released from pristine AB and synthesized AB@$M_{1.5}$ sample, which was obtained by loading AB to the template of $M_{1.5}$. The $M_{1.5}$ was selected as the template to support AB due to its uniform and regular spherical morphology. As shown in Figure 8a, pristine AB can release the first equivalent and the second equivalent of H_2 at the temperatures of ∼110 and 150 °C, respectively, whereas the AB@$M_{1.5}$ sample starts to evolve H_2 at ∼70 °C with a broad peak centered at 90 °C, which is ∼40 °C lower than those for pristine AB. Another notable effect resulting from the MS curves is the evolution of the borazine, ammonia, and diborane

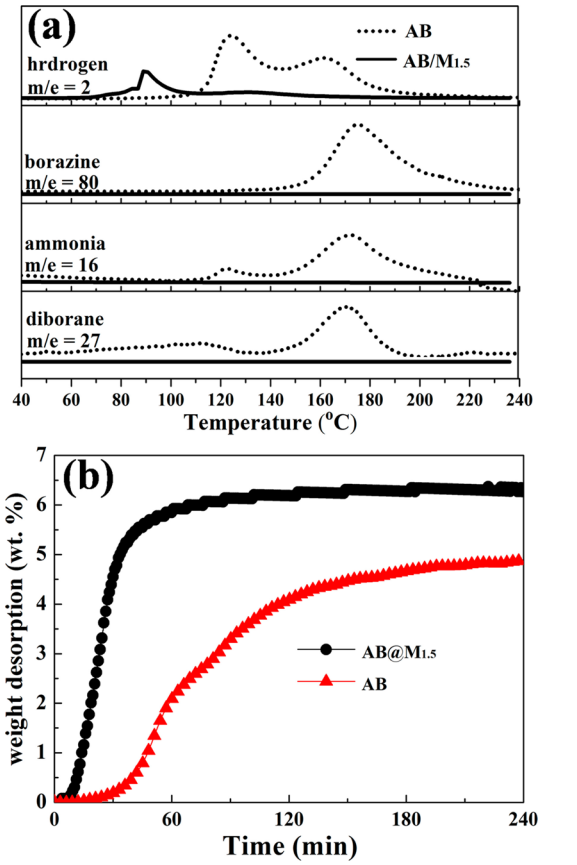

Figure 8. (a) MS results of AB@$M_{1.5}$ between 40 and 240 °C at a heating rate of 5 °C min^{-1}. (b) Isothermal volumetric hydrogen release properties of AB@$M_{1.5}$ and pristine AB at 90 °C.

byproducts (m/z = 80, m/z = 16, and m/z = 27) that are depressed completely for AB@$M_{1.5}$, which is more predominant than most of the previous reports.[61,64] The isothermal volumetric hydrogen release properties of the pristine AB and AB@$M_{1.5}$ sample were measured at 90 °C to compare the gas release rate as well as the hydrogen release kinetics (Figure 8b). Clearly, sluggish gas desorption and only 4.8 wt % weight desorption up to 200 min are observed for pristine AB, which may be ascribed to its high kinetic barrier for dehydrogenation at this temperature. In contrast, vigorous hydrogen release without any induction period could be observed from the AB@$M_{1.5}$ sample at the same temperature. A total gas capacity of 0.03 mol g^{-1} (based on the weight of pristine AB) in 60 min could be detected from isothermal volumetric release result of AB@$M_{1.5}$. Due to the complete suppression of the borazine, ammonia, and diborane byproducts, hydrogen is the only material released in this process. Therefore, the weight desorption (∼6.0 wt %) can be calculated based on the product of multiplying the total gas capacity (0.03 mol g^{-1}) and the molar mass of hydrogen (2.016 g mol^{-1}), as shown in Figure 8b. It is clear that the improved dehydrogenation properties and hydrogen release kinetics, as well as the complete depression of the release of undesired volatile byproducts, are achieved successfully for the AB@$M_{1.5}$ composite compared with neat AB. Such significantly improved dehydrogenation properties of AB@$M_{1.5}$ may be contributed to the confinement of AB in the MOFs nanoscaffolds as well as the probable catalytic effect of Ni ions from Ni-MOFs.[64]

DOI: 10.1021/acssuschemeng.5b00556
ACS Sustainable Chem. Eng. 2015, 3, 1830−1838

CONCLUSIONS

In summary, a facile and fast microwave hydrothermal method was used to fabricate Ni-MOFs in this work. The Ni-MOFs were used as the precursor to obtain mesoporous yolk−shell NiO microspheres or as the matrix to load AB. The yolk−shell NiO@NiO microsphere exhibits a large reversible capacity of 1063 mAh g^{-1} at 0.2 A g^{-1} along with a good high-rate capability. Moreover, the hydrogen desorption properties of the Ni-MOFs supported AB composite have also been investigated. It delivers a lower temperature for the first-step dehydrogenation, improved dehydrogenation rate, and complete depression of the release of byproducts. The MOF-based synthesis and application strategy can be extended to synthesize other metals/metal oxides for applications in lithium-ion batteries or hydrogen desorption.

ASSOCIATED CONTENT

Supporting Information

Representative cyclic voltammograms (CVs), first-three discharge and charge curves, TEM image of NiO materials, and table showing the property comparison with other NiO nanostructures. The Supporting Information is available free of charge on the ACS Publications website at DOI: 10.1021/acssuschemeng.5b00556.

AUTHOR INFORMATION

Corresponding Authors

*E-mail: vivisun@shu.edu.cn. Telephone: +86-21-66137483. Fax: +86-21-66137725 (W. Sun).

*E-mail: yongwang@shu.edu.cn. Telephone: +86-21-66137723. Fax: +86-21-66137725 (Y. Wang).

Notes

The authors declare no competing financial interest.

ACKNOWLEDGMENTS

The authors gratefully acknowledge the follow-up Program for Professor of Special Appointment in Shanghai (Eastern Scholar), National Natural Science Foundation of China (51271105 and 51201095), Shanghai Municipal Education Commission (13YZ012), and Innovative Research Team (IRT13078) for financial support. The authors also thank the Lab for Microstructure, Instrumental Analysis and Research Center, Shanghai University, for materials characterizations.

REFERENCES

(1) Li, L.; Wu, Z.; Yuan, S.; Zhang, X. B. Advances and challenges for flexible energy storage and conversion devices and systems. *Energy Environ. Sci.* **2014**, *7*, 2101−2122.

(2) Zhang, Q. F.; Uchaker, E.; Candelaria, S. L.; Cao, G. Z. Nanomaterials for energy conversion and storage. *Chem. Soc. Rev.* **2013**, *42*, 3127−3171.

(3) Zhu, J. X.; Yang, D.; Yin, Z. Y.; Yan, Q. Y.; Zhang, H. Graphene and graphene-based materials for energy storage applications. *Small* **2014**, *10*, 3480−3498.

(4) Dutta, S.; Bhaumik, A.; Wu, K. C. W. Hierarchically porous carbon derived from polymers and biomass: effect of interconnected pores on energy applications. *Energy Environ. Sci.* **2014**, *7*, 3574−3592.

(5) Kim, H.; Hong, J.; Park, K. Y.; Kim, H.; Kim, S. W.; Kang, K. Aqueous rechargeable Li and Na ion batteries. *Chem. Rev.* **2014**, *114*, 11788−11827.

(6) Mai, L. Q.; Tian, X. C.; Xu, X.; Chang, L.; Xu, L. Nanowire electrodes for electrochemical energy storage devices. *Chem. Rev.* **2014**, *114*, 11828−11862.

(7) Titirici, M. M.; White, R. J.; Brun, N.; Budarin, V. L.; Su, D. S.; del Monte, F.; Clark, J. H.; MacLachlan, M. J. Sustainable carbon materials. *Chem. Soc. Rev.* **2015**, *44*, 250−290.

(8) Sun, W. W.; Wang, Y. Graphene-based nanocomposite anodes for lithium-ion batteries. *Nanoscale* **2014**, *6*, 11528−11552.

(9) Wang, X. F.; Lu, X. H.; Liu, B.; Chen, D.; Tong, Y. X.; Shen, G. Z. Flexible energy-storage devices: design consideration and recent progress. *Adv. Mater.* **2014**, *26*, 4763−4782.

(10) Xia, X. H.; Zhang, Y. Q.; Chao, D. L.; Guan, C.; Zhang, Y. J.; Li, L.; Ge, X.; Bacho, I. M.; Tu, J. P.; Fan, H. J. Solution synthesis of metal oxides for electrochemical energy storage applications. *Nanoscale* **2014**, *6*, 5008−5048.

(11) Li, X. F.; Wang, C. L. Engineering nanostructured anodes via electrostatic spray deposition for high performance lithium ion battery application. *J. Mater. Chem. A* **2013**, *1*, 165−182.

(12) Ren, Y. Q.; Chia, G. H.; Gao, Z. Q. Metal-organic frameworks in fuel cell technologies. *Nano Today* **2013**, *8*, 577−597.

(13) Garbayo, I.; Pla, D.; Morata, A.; Fonseca, L.; Sabaté, N.; Tarancón, A. Full ceramic micro solid oxide fuel cells: towards more reliable MEMS power generators operating at high temperatures. *Energy Environ. Sci.* **2014**, *7*, 3617−3629.

(14) Yoon, D.; Manthiram, A. Hydrocarbon-fueled solid oxide fuel cells with surface-modified, hydroxylated Sn/Ni-$Ce_{0.8}Gd_{0.2}O_{1.9}$ heterogeneous catalyst anode. *J. Mater. Chem. A* **2014**, *2*, 17041−17046.

(15) Jung, W.; Gu, K. L.; Choi, Y.; Haile, S. M. Robust nanostructures with exceptionally high electrochemical reaction activity for high temperature fuel cell electrodes. *Energy Environ. Sci.* **2014**, *7*, 1685−1692.

(16) Sculley, J.; Yuan, D. Q.; Zhou, H. C. The current status of hydrogen storage in metal-organic frameworks-updated. *Energy Environ. Sci.* **2011**, *4*, 2721−2735.

(17) Geng, H.; Kong, S. F.; Wang, Y. NiS nanorods-assembled nanoflower grown on graphene: morphology evolution and Li-ion storage application. *J. Mater. Chem. A* **2014**, *2*, 15152−15158.

(18) Kong, S. F.; Jin, Z. T.; Liu, H.; Wang, Y. Morphological effect of graphene nanosheets on ultrathin CoS nanosheets and their applications for high-performance Li-ion batteries and photocatalysis. *J. Phys. Chem. C* **2014**, *118*, 25355−25364.

(19) Bai, Z. C.; Ju, Z. C.; Guo, C. L.; Qian, Y. T.; Tang, B.; Xiong, S. L. Direct large-scale synthesis of 3D hierarchical mesoporous NiO microspheres as high-performance anode materials for lithium ion batteries. *Nanoscale* **2014**, *6*, 3268−3273.

(20) Zhu, Y. Q.; Guo, H. Z.; Wu, Y.; Cao, C. B.; Tao, S.; Wu, Z. Y. Surface-enabled superior lithium storage of high-quality ultrathin NiO nanosheets. *J. Mater. Chem. A* **2014**, *2*, 7904−7911.

(21) Su, D. W.; Ford, M.; Wang, G. X. Mesoporous NiO crystals with dominantly exposed {110} reactive facets for ultrafast lithium storage. *Sci. Rep.* **2012**, *2*, 924.

(22) Wang, X. H.; Qiao, L.; Sun, X. L.; Li, X. W.; Hu, D. K.; Zhang, Q.; He, D. Y. Mesoporous NiO nanosheet networks as high performance anodes for Li ion batteries. *J. Mater. Chem. A* **2013**, *1*, 4173−4176.

(23) Choi, S. H.; Kang, Y. C. Ultrafast synthesis of yolk-shell and cubic NiO nanopowders and application in lithium ion batteries. *ACS Appl. Mater. Interfaces* **2014**, *6*, 2312−2316.

(24) Zhang, G. H.; Chen, Y. J.; Qu, B. H.; Hu, L. L.; Mei, L.; Lei, D. N.; Li, Q.; Chen, L. B.; Li, Q. H.; Wang, T. H. Synthesis of mesoporous NiO nanospheres as anode materials for lithium ion batteries. *Electrochim. Acta* **2012**, *80*, 140−147.

(25) Wang, X. H.; Yang, Z. B.; Sun, X. L.; Li, X. W.; Wang, D. S.; Wang, P.; He, D. Y. NiO nanocone array electrode with high capacity and rate capability for Li-ion batteries. *J. Mater. Chem.* **2011**, *21*, 9988−9990.

(26) Wang, N. N.; Chen, L.; Ma, X. J.; Yue, J.; Niu, F. E.; Xu, H. Y.; Yang, J.; Qian, Y. T. Facile synthesis of hierarchically porous NiO microtubes as advanced anode materials for lithium-ion batteries. *J. Mater. Chem. A* **2014**, *2*, 16847−16850.

(27) Xie, D.; Yuan, W. W.; Dong, Z. M.; Su, Q. M.; Zhang, J.; Du, G. H. Facile synthesis of porous NiO hollow microspheres and its

electrochemical lithium-storage performance. *Electrochim. Acta* **2013**, *92*, 87−92.
(28) Kawamori, M.; Asai, T.; Shirai, Y.; Yagi, S.; Oishi, M.; Ichitsubo, T.; Matsubara, E. Three-dimensional nanoelectrode by metal nanowire nonwoven clothes. *Nano Lett.* **2014**, *14*, 1932−1937.
(29) Xie, D.; Su, Q. M.; Dong, Z. M.; Zhang, J.; Du, G. H. L-cysteine-assisted preparation of porous NiO hollow microspheres with enhanced performance for lithium storage. *CrystEngComm* **2013**, *15*, 8314−8319.
(30) Sasidharan, M.; Gunawardhana, N.; Senthil, C.; Yoshio, M. Micelle templated NiO hollow nanospheres as anode materials in lithium ion batteries. *J. Mater. Chem. A* **2014**, *2*, 7337−7344.
(31) Pan, J. H.; Huang, Q. Z.; Koh, Z. Y.; Neo, D.; Wang, X. Z.; Wang, Q. Scalable synthesis of urchin- and flowerlike hierarchical NiO microspheres and their electrochemical property for lithium storage. *ACS Appl. Mater. Interfaces* **2013**, *5*, 6292−6299.
(32) Wang, B.; Cheng, J. L.; Wu, Y. P.; Wang, D.; He, D. N. Porous NiO fibers prepared by electrospinning as high performance anode materials for lithium ion batteries. *Electrochem. Commun.* **2012**, *23*, 5−8.
(33) Guo, H.; Wang, Y. P.; Wang, W.; Liu, L. X.; Guo, Y. Y.; Yang, X. J.; Wang, S. X. Template-free fabrication of hollow NiO-carbon hybrid nanoparticle aggregates with improved lithium storage. *Part. Part. Syst. Charact.* **2014**, *31*, 374−381.
(34) Ni, Y. M.; Yin, Y. J.; Wu, P.; Zhang, H.; Cai, C. X. Nitrogen/carbon atomic ratio-dependent performances of nitrogen-doped carbon-coated metal oxide nanocrystals for anodes in lithium-ion batteries. *ACS Appl. Mater. Interfaces* **2014**, *6*, 7346−7355.
(35) Susantyoko, R. A.; Wang, X. H.; Xiao, Q. Z.; Fitzgerald, E.; Zhang, Q. Sputtered nickel oxide on vertically-aligned multiwall carbon nanotube arrays for lithium-ion batteries. *Carbon* **2014**, *68*, 619−627.
(36) Zhuo, L. H.; Wu, Y. Q.; Zhou, W.; Wang, L. Y.; Yu, Y. C.; Zhang, X. B.; Zhao, F. Y. Trace amounts of water-induced distinct growth behaviors of NiO nanostructures on graphene in CO_2-expanded ethanol and their applications in lithium-ion batteries. *ACS Appl. Mater. Interfaces* **2013**, *5*, 7065−7071.
(37) Lee, D. H.; Kim, J. C.; Shim, H. W.; Kim, D. W. Highly reversible Li storage in hybrid NiO/Ni/graphene nanocomposites prepared by an electrical wire explosion process. *ACS Appl. Mater. Interfaces* **2014**, *6*, 137−142.
(38) Zhou, G. M.; Wang, D. W.; Yin, L. C.; Li, N.; Li, F.; Cheng, H. M. Oxygen bridges between NiO nanosheets and graphene for improvement of lithium storage. *ACS Nano* **2012**, *6*, 3214−3223.
(39) Choi, S. H.; Ko, Y. N.; Lee, J. K.; Kang, Y. C. Rapid continuous synthesis of spherical reduced graphene ball-nickel oxide composite for lithium ion batteries. *Sci. Rep.* **2014**, *4*, 5786.
(40) Zou, Y. Q.; Wang, Y. NiO nanosheets grown on graphene nanosheets as superior anode materials for Li-ion batteries. *Nanoscale* **2011**, *3*, 2615−2620.
(41) Xie, D.; Su, Q. M.; Yuan, W. W.; Dong, Z. M.; Zhang, J.; Du, G. H. Synthesis of porous NiO-wrapped graphene nanosheets and their improved lithium storage properties. *J. Phys. Chem. C* **2013**, *117*, 24121−24128.
(42) Wen, W.; Wu, J. M. Eruption combustion synthesis of NiO/Ni nanocomposites with enhanced properties for dye-absorption and lithium storage. *ACS Appl. Mater. Interfaces* **2011**, *3*, 4112−4119.
(43) Liu, C.; Li, F.; Ma, L. P.; Cheng, H. M. Advanced materials for energy storage. *Adv. Mater.* **2010**, *22*, E28−E62.
(44) Gao, F.; Zhao, G. L.; Yang, S. Z.; Spivey, J. J. Nitrogen-doped fullerene as a potential catalyst for hydrogen fuel cells. *J. Am. Chem. Soc.* **2013**, *135*, 3315−3318.
(45) Grochala, W.; Edwards, P. P. Thermal decomposition of the non-interstitial hydrides for the storage and production of hydrogen. *Chem. Rev.* **2004**, *104*, 1283−1315.
(46) Yang, J.; Sudik, A.; Wolverton, C.; Siegel, D. J. High capacity hydrogen storage materials: attributes for automotive applications and techniques for materials discovery. *Chem. Soc. Rev.* **2010**, *39*, 656−675.
(47) Li, L.; Yao, X. D.; Sun, C. H.; Du, A. J.; Cheng, L. N.; Zhu, Z. H.; Yu, C. Z.; Zou, J.; Smith, S. C.; Wang, P.; Cheng, H. M.; Frost, R. L.; Lu, G. Q. Lithium-catalyzed dehydrogenation of ammonia borane within mesoporous carbon framework for chemical hydrogen storage. *Adv. Funct. Mater.* **2009**, *19*, 265−271.
(48) Li, J.; Zhu, Q. L.; Xu, Q. Highly active AuCo alloy nanoparticles encapsulated in the pores of metal-organic frameworks for hydrolytic dehydrogenation of ammonia borane. *Chem. Commun.* **2014**, *50*, 5899−5901.
(49) Chen, X. W.; Wan, L.; Huang, J. M.; Ouyang, L. Z.; Zhu, M.; Guo, Z. P.; Yu, X. B. Nitrogen-containing carbon nanostructures: a promising carrier for catalysis of ammonia borane dehydrogenation. *Carbon* **2014**, *68*, 462−472.
(50) Yao, Q. L.; Lu, Z. H.; Zhang, Z. J.; Chen, X. S.; Lan, Y. Q. One-pot synthesis of core-shell Cu@SiO_2 nanospheres and their catalysis for hydrolytic dehydrogenation of ammonia borane and hydrazine borane. *Sci. Rep.* **2014**, *4*, 7597.
(51) Rowsell, J. L. C.; Yaghi, O. M. Strategies for hydrogen storage in metal−organic frameworks. *Angew. Chem., Int. Ed.* **2005**, *44*, 4670−4679.
(52) Li, S. L.; Xu, Q. Metal-organic frameworks as platforms for clean energy. *Energy Environ. Sci.* **2013**, *6*, 1656−1683.
(53) Zhang, L.; Wu, H. B.; Madhavi, S.; Hng, H. H.; Lou, X. W. Formation of Fe_2O_3 microboxes with hierarchical shell structures from metal-organic frameworks and their lithium storage properties. *J. Am. Chem. Soc.* **2012**, *134*, 17388−17391.
(54) Liu, L. X.; Guo, H.; Liu, J. J.; Qian, F.; Zhang, C. H.; Li, T. T.; Chen, W. W.; Yang, X. J.; Guo, Y. C. Self-assembled hierarchical yolk-shell structured NiO@C from metal-organic frameworks with outstanding performance for lithium storage. *Chem. Commun.* **2014**, *50*, 9485−9488.
(55) Hu, L.; Huang, Y. M.; Zhang, F. P.; Chen, Q. W. CuO/Cu_2O composite hollow polyhedrons fabricated from metal-organic framework templates for lithium-ion battery anodes with a long cycling life. *Nanoscale* **2013**, *5*, 4186−4190.
(56) Shao, J.; Wan, Z. M.; Liu, H. M.; Zheng, H. Y.; Gao, T.; Shen, M.; Qu, Q. T.; Zheng, H. H. Metal organic frameworks-derived Co_3O_4 hollow dodecahedrons with controllable interiors as outstanding anodes for Li storage. *J. Mater. Chem. A* **2014**, *2*, 12194−12200.
(57) Lü, Y. Y.; Zhan, W. W.; He, Y.; Wang, Y. T.; Kong, X. J.; Kuang, Q.; Xie, Z. X.; Zheng, L. S. MOF-templated synthesis of porous Co_3O_4 concave nanocubes with high specific surface area and their gas sensing properties. *ACS Appl. Mater. Interfaces* **2014**, *6*, 4186−4195.
(58) Xu, X. D.; Cao, R. G.; Jeong, S.; Cho, J. Spindle-like mesoporous α-Fe_2O_3 anode material prepared from MOF template for high-rate lithium batteries. *Nano Lett.* **2012**, *12*, 4988−4991.
(59) Banerjee, A.; Singh, U.; Aravindan, V.; Srinivasan, M.; Ogale, S. Synthesis of CuO nanostructures from Cu-based metal organic framework (MOF-199) for application as anode for Li-ion batteries. *Nano Energy* **2013**, *2*, 1158−1163.
(60) Hu, L.; Chen, Q. W. Hollow/porous nanostructures derived from nanoscale metal-organic frameworks towards high performance anodes for lithium-ion batteries. *Nanoscale* **2014**, *6*, 1236−1257.
(61) Gao, L.; Li, C. Y. V.; Yung, H.; Chan, K. Y. A functionalized MIL-101(Cr) metal-organic framework for enhanced hydrogen release from ammonia borane at low temperature. *Chem. Commun.* **2013**, *49*, 10629−10631.
(62) Zhong, R. Q.; Zou, R. Q.; Nakagawa, T.; Janicke, M.; Semelsberger, T. A.; Burrell, A. K.; Del Sesto, R. E. Improved hydrogen release from ammonia-borane with ZIF-8. *Inorg. Chem.* **2012**, *51*, 2728−2730.
(63) Srinivas, G.; Travis, W.; Ford, J.; Wu, H.; Guo, Z. X.; Yildirim, T. Nanoconfined ammonia borane in a flexible metal-organic framework Fe-MIL-53: clean hydrogen release with fast kinetics. *J. Mater. Chem. A* **2013**, *1*, 4167−4172.
(64) Si, X. L.; Sun, L. X.; Xu, F.; Jiao, C. L.; Li, F.; Liu, S. S.; Zhang, J.; Song, L. F.; Jiang, C. H.; Wang, S.; Liu, Y. L.; Sawada, Y. Improved hydrogen desorption properties of ammonia borane by Ni-modified

DOI: 10.1021/acssuschemeng.5b00556
ACS Sustainable Chem. Eng. 2015, 3, 1830−1838

metal-organic frameworks. *Int. J. Hydrogen Energy* **2011**, *36*, 6698−6704.

DOI: 10.1021/acssuschemeng.5b00556
ACS Sustainable Chem. Eng. 2015, 3, 1830−1838